The Astrophysical Journal, 988:181 (11pp), 2025 August 1 https://doi.org/10.3847/1538-4357/ade2e2

Multispacecraft Observations of the 27 Day Periodicity in Galactic Protons from 2018 to 2019

S. Amoroso[1,2], M. Babu[3,4], S. Bartocci[5], R. Battiston[3,4], S. Beolè[6,7], W. J. Burger[4], D. Campana[8], P. Cipollone[2], L. Conti[2,9], A. Contin[10,11], M. Cristoforetti[4,12], C. De Donato[2], C. De Santis[2], A. Di Luca[4,12], F. M. Follega[3,4], G. Gebbia[3,4], R. Iuppa[3,4], A. Lega[3,4], M. Lolli[11], M. Martucci[2], G. Masciantonio[2], M. Mergè[13], M. Mese[8,14], C. Neubüser[4], R. Nicolaidis[3,4], F. Nozzoli[4], A. Oliva[11], G. Osteria[8], F. Palma[2], B. Panico[8,14], F. Perfetto[8], A. Perinelli[3,4], P. Picozza[1,2], S. Pietroni[1,2], M. Pozzato[11], E. Ricci[3,4], L. Ricci[3,4], M. Ricci[2,15], S. B. Ricciarini[16], Z. Sahnoun[10,11], U. Savino[6,7], V. Scotti[8,14], M. Sorbara[1,2], A. Sotgiu[2], R. Sparvoli[1,2], P. Ubertini[17], V. Vilona[4], S. Zoffoli[13], P. Zuccon[3,4], M. Boezio[18,19], R. Munini[18,19], O. P. M. Aslam[20], X. Luo[21], D. C. Ndiitwani[22], M. D. Ngobeni[22,23], M. Piersanti[17,24], M. S. Potgieter[25], and I. I. Ramokgaba[22]

[1] Università di Roma Tor Vergata, V. della Ricerca Scientifica 1, 00133, Rome, Italy
[2] INFN—Sezione di Roma Tor Vergata, V. della Ricerca Scientifica 1, 00133, Rome, Italy; matteo.martucci@roma2.infn.it, francesco.palma@roma2.infn.it
[3] Università di Trento, V. Sommarive 14, 38123 Povo (TN), Italy
[4] INFN–TIFPA, V. Sommarive 14, 38123 Povo (TN), Italy
[5] INFN–AC, Via E. Fermi 54, 00044 Frascati (RM), Italy
[6] Università di Torino, V. P. Giuria 1, 10125, Turin, Italy
[7] INFN–Sezione di Torino, V. P. Giuria 1, 10125, Turin, Italy
[8] INFN–Sezione di Napoli, V. Cintia, 80126, Naples, Italy
[9] Uninettuno University, C.so V. Emanuele II, 39, I-00186, Rome, Italy
[10] Università di Bologna, V.le Berti Pichat 6/2, Bologna, Italy
[11] INFN–Sezione di Bologna, V.le Berti Pichat 6/2, Bologna, Italy
[12] Fondazione Bruno Kessler, V. Sommarive 18, 38123, Povo (TN), Italy
[13] Italian Space Agency, V. del Politecnico, I-00133, Rome, Italy
[14] Università degli Studi di Napoli Federico II, V. Cintia, 80126, Naples, Italy
[15] INFN–LNF, V. E. Fermi 54, 00044 Frascati (RM), Italy
[16] IFAC-CNR, V. Madonna del Piano 10, 50019 Sesto Fiorentino (FI), Italy
[17] INAF-IAPS, V. Fosso del Cavaliere 100, 00133, Rome, Italy
[18] INFN, Sezione di Trieste, 34149 Trieste, Italy
[19] IFPU, I-34014 Trieste, Italy
[20] School of Mathematics and Statistics, University of Glasgow, Glasgow G12 8QQ, UK
[21] Shandong Institute of Advanced Technology (SDIAT), 250100 Jinan, Shandong, People's Republic of China
[22] Centre for Space Research, North-West University, 2520 Potchefstroom, South Africa
[23] Department of Physical and Earth Sciences, Sol Plaatje University, Private Bag X5008, Kimberley 8301, South Africa
[24] Università dell'Aquila, V. Vetoio 42, 67100, Coppito (AQ), Italy
[25] Institute for Experimental and Applied Physics (IEAP), Christian-Albrechts University in Kiel, D-24118 Kiel, Germany
Received 2025 February 17; revised 2025 May 26; accepted 2025 June 7; published 2025 July 23

Abstract

Galactic cosmic-ray (GCR) intensities exhibit recurrent variations caused by their passage through plasma interaction regions corotating with the Sun, with the ∼27 day periodicity being the most prominent one. Data collected by the High-Energy Particle Detector (HEPD-01) on board the China Seismo-Electromagnetic Satellite in Low-Earth Orbit have been used to derive daily proton fluxes from 2018 to 2019 August, in the energy range between ∼55 and ∼200 MeV. Daily fluxes from HEPD-01 have been analyzed along with proton fluxes measured during the same period by ERNE and EPHIN, on board the SOHO spacecraft, and by AMS-02, on board the International Space Station. Using a time-frequency analysis, we confirm a slight energy dependence for the power of the ∼27 day variation as a function of time, with the periodicity maximum occurring earlier for HEPD-01 than for high-energy data from AMS-02. Additionally, as already obtained in previous studies, the rigidity dependence of the amplitude of the aforementioned GCR variation cannot be described by the same power law at both low and high energies, as a consequence of different physical mechanisms playing roles at different rigidity ranges. HEPD-01 GCR measurements cover the energy range from tens to a few hundreds of MeV, which is not accessible to existing detectors (EPHIN and ERNE covering from a few MeV up to tens or a hundred MeV, respectively, and AMS-02 in the GeV–TeV energy range), providing important information for understanding GCR periodicities.

Unified Astronomy Thesaurus concepts: Galactic cosmic rays (567); Heliosphere (711); Cosmic ray detectors (325)

1. Introduction

Galactic cosmic rays (GCRs) observed near Earth are known to be affected by a plethora of factors during their passage through the heliosphere. After entering this region, GCRs are continuously modulated by the change in the solar

wind (SW) and the associated heliospheric magnetic field (HMF). Magnetic fields and processes such as diffusion, convection, and drifts affect cosmic particles on different timescales (from hours to several years) and with various intensities corresponding to the solar activity, resulting in cosmic-ray intensity variations (E. N. Parker 1965; M. S. Potgieter 2013a, 2013b; G. Bazilevskaya et al. 2014; K. Kudela & I. Sabbah 2015; P. Chowdhury et al. 2016). These variations decrease with increasing energy and are particularly visible at energies below 100 GeV. The two different types of GCR variations—observable at both ground and space levels—are nonrecurrent and recurrent variations. The former include the so-called Forbush decreases, which are sudden, short-lived (from days to weeks) drops in GCR intensity caused by the passage of coronal mass ejections (CMEs) through Earth's magnetosphere (S. E. Forbush 1938; H. V. Cane 2000). Conversely, recurrent variations (or periodicities) are well connected to the solar cycle (SC) and geometry of the Sun–Earth connection, and cause minor effects on human-related activities. The most significant periodic variations are the 22 yr, 11 yr, ∼27 day, and the solar diurnal variation (24 hr). The long-term solar modulations of 22 yr and 11 yr (M. S. Potgieter 2017; I. G. Usoskin 2017) are connected with the global HMF and the solar activity cycle, respectively. During the 11 yr SC, the number of sunspots changes from minimum to maximum and then back to a minimum (D. H. Hathaway 2015), and is known to be anticorrelated with the GCR flux, with some time delay caused by irregularities in the interplanetary magnetic field (A. López-Comazzi & J. Blanco 2022 and references therein).

The GCR recurrent variation with a period of ∼27 days, which is the main topic of this paper, is related to the passage of corotating interaction regions (CIRs) originating from one or more coronal holes of the Sun (J. A. Simpson 1998; I. G. Richardson 2004, 2018). These long-lasting, relatively large-scale plasma structures—generated in low- and medium-latitude regions of the inner heliosphere—are the manifestation of the interactions of fast SW streams with the slow SW. These high-speed streams (J. Phillips et al. 1995; M. Neugebauer & C. W. Snyder 1966; B. Tsurutani et al. 2006), originating from coronal holes (A. S. Krieger et al. 1973), are corotating while flowing radially outward, and when they overtake the surrounding slower-speed SW, they also create forward and reverse shocks along the CIR, which may accelerate particles up to 20 MeV nucleon^{-1}. CIR forward shocks generally form beyond ∼2 au from the Sun (E. J. Smith & J. H. Wolfe 1976). The Sun rotates on its axis at different rates depending on the heliolatitudes: the period of the solar rotation is 25–26 days and 36 days at the equatorial/near equatorial and polar regions, respectively. However, for an observer on Earth, this periodicity equals ∼27 days because of the orbital motion of Earth. This is called the solar synodic rotation period. Historically, the important role of non-axisymmetric magnetic fields in the origin of solar phenomena has been assessed (A. Bigazzi & A. Ruzmaikin 2004). More recently, some results suggested that Rossby waves contribute to the organization and propagation of various photospheric magnetic features—like CIRs—on the timescale of several months (B. Raphaldini et al. 2023). From a spatial point of view, CIRs and their associated shocks can spread over several astronomical units (∼3–6 au) and, consequently, a ∼27 day variation arises in the GCR flux, which persists over several months. The ∼27 day GCR variations were observed not only on Earth by ground-based neutron monitors (NMs; see A. Gil & K. Mursula 2017 and A. López-Comazzi & J. Blanco 2022), but also near Earth by several space missions (ACE and SOHO P. Kotzé 2023; PAMELA R. Modzelewska et al. 2020; AMS-02 M. Aguilar et al. 2021, and others), in the inner heliosphere out of the ecliptic plane by Ulysses (H. Kunow et al. 1995; R. B. McKibben et al. 1995; B. Heber et al. 1999; B. Heber & M. S. Potgieter 2006), and even in the outer heliosphere by the Voyager spacecraft (R. Decker 1999). These effects on GCRs are especially prominent during the declining phase of the SC, but not exclusively so, depending on solar activity conditions applicable to GCRs at different phases of the SC. They usually seem to occur at low heliolatitudes, where the HMF has a well-established sector structure and coronal holes spread to lower heliolatitudes. These conditions usually prevail in periods near SC minima. Consequently, the characteristic ∼27 day GCR variation is thus mostly evident during the minimum and near-minimum epochs of solar activity and may last over relatively long periods, even up to about 1 yr, as reported in M. Aguilar et al. (2021).

Despite the ∼27 days, GCR variations have been a widely studied topic; some peculiar features are still under study, such as their HMF polarity dependence and their dependence on the particle's rigidity over a wide rigidity (energy) range.

I. G. Richardson et al. (1999) showed for the first time that the amplitude of the ∼27 day GCR variation (which is the value of the maximum decrease of these GCR variations) is larger when $A > 0$ than during adjacent minima when $A<0$, where A is the global direction of the HMF. This polarity dependence was confirmed by R. Modzelewska & A. Gil (2021) for the ∼27 day variations of the GCR anisotropy and intensity observed by NMs in the solar minima 23/24 (2007–2009) and 24/25 (2017–2019). However, in the same work, the ∼27 day variations of lower energy (<1 GeV) GCR protons registered by STEREO A and B and SOHO/EPHIN and high-mass species by ACE/CRIS observed in the solar minima 23/24 and 24/25 remain at the same level and seem not to be polarity dependent. In addition, the authors conclude that recurrent variations connected with the solar rotation for low-energy (<1 GeV) cosmic rays may be relatively more sensitive to the enhanced diffusion effects, leading to the same level of the ∼27 day amplitudes for the $A > 0$ and $A < 0$ polarities. At high-energy (>1 GeV) cosmic rays, as observed by NMs, exhibit a large-scale drift effect, resulting in the 22 yr Hale cycle of the ∼27 day GCR variations, with larger amplitudes in the $A > 0$ polarity than in $A < 0$. Conversely, P. Kotzé (2023) recently revealed strong evidence that the ∼27 day periodicity in proton, C and O GCR particles as measured by SOHO/EPHIN and ACE/CRIS during SC 23 and SC 24, as well as NM observations at the Oulu, Hermanus, and Tsumeb stations, experience an increase in power during time intervals characterized by a positive solar polarity in contrast to intervals with negative solar polarity. In spite of the progress that has been made from the experimental and theoretical point of view in understanding the modulation processes governing the ∼27 day variation of the GCR intensity and anisotropy, the problem is not entirely solved to date, and more sophisticated numerical models (e.g., A. Wawrzynczak et al. 2015; X. Guo & V. Florinski 2016; T. Wiengarten et al. 2016; A. Kopp et al. 2017; X. Luo et al. 2020) will be validated on this issue in the future.

Of particular interest is also how the amplitude of the ∼27 day variation depends on particle rigidity, as studied by R. Modzelewska et al. (2020) in GCR fluxes during the prolonged 2007–2008 solar minimum between SC 23 and SC 24 using space-based PAMELA (P. Picozza et al. 2007) and ARINA (A. Bakaldin et al. 2007) proton data in a wide rigidity range from $R \sim 0.3$ GV to $R \sim 10$ GV. According to PAMELA and ARINA data, the rigidity dependence of the amplitude of the ∼27 day GCR variations cannot be described by the same power law at both low and high rigidities, showing a flat maximum in the region of 1 GV and a power-law mode with an index $\gamma \approx -0.5$ for $R \geqslant 1$ GV. Unfortunately, a direct quantitative comparison between these results and NM observations is not correct, since NMs are integral detectors and respond to particle energies above several GVs. NM studies on the estimated rigidity dependence in periodicities, for example, in A. López-Comazzi & J. Blanco (2022) generally concluded that the power of the periodicity decreases with increasing rigidity. This formed the paradigm over the AMS-02 rigidity range (1.71–100 GV) that the strength of the ∼27 day periodicities (and submultiple periods of 13.5 and 9 days) steadily decreases with increasing rigidity of cosmic rays, differently in solar maximum and minimum (A. Gil & M. V. Alania 2013). However, recent AMS-02 results on periodicities in the daily proton fluxes up to 100 GV over an extended period from 2011 to 2019 (M. Aguilar et al. 2021) do not support that the strength of all the periodicities would always decrease with increasing rigidity. Indeed, the strength of 9 day and 13.5 day periodicities unexpectedly increases with increasing rigidity up to ∼10 GV and ∼20 GV, respectively, and then decreases with increasing rigidity up to 100 GV. Moreover, the rigidity dependence of the ∼27 day periodicity varies in different time intervals and is different from the rigidity dependences of 9 day and 13.5 day periods.

In this paper, we present the results of the ∼27 day variation in GCR protons with energies from 55 to 200 MeV as observed by the High-Energy Particle Detector (HEPD-01) on board the China Seismo-Electromagnetic Satellite (CSES-01) between 2018 August and 2019. HEPD-01 observations fill the largely unexplored energy gap between the GCR particles detected in space by low-energy (SOHO/EPHIN, SOHO/ERNE, etc., from a few MeV to ∼100 MeV) and higher-energy (e.g., PAMELA and AMS-02 in the GeV–TeV range) experiments. Moreover, they can be used to test the numerical modeling of the CIR effects on GCR transport (e.g., X. Luo et al. 2024). HEPD-01 data—together with those of its successor (HEPD-02) planned to be launched in 2025 June—may thus contribute to further understanding the mechanism of the ∼27 day GCR variation.

2. HEPD-01 Detector for the CSES-Limadou Mission

The space-borne HEPD-01 detector—developed and assembled in Italy as part of the Limadou branch of the CSES project—is a rather new addition to the network of spacecraft monitoring the near-Earth environment. It serves as one of the nine devices on board CSES-01, launched in 2018 and put in a low-Earth Sun-synchronous polar orbit at ∼500 km, 97° inclination, and ∼5 day revisiting periodicity (X. Shen et al. 2018). These instruments were designed to study electromagnetic field, wave, plasma, and particle perturbations in the ionosphere and magnetosphere, induced by either natural sources (earthquakes, solar events, cosmic rays, etc.) or artificial emitters. HEPD-01 is a lightweight (∼45 kg) and compact ($40.36 \times 53.00 \times 38.15$ cm^3) payload, containing—from top to bottom—a tracker made up of two double-sided silicon microstrip planes ($213.2 \times 214.8 \times 0.3$ mm^3), a trigger system including one EJ-200 plastic scintillator layer segmented into six paddles ($20 \times 3 \times 0.5$ cm^3 each), a range calorimeter comprising a stack (TOWER) of 16 plastic scintillator planes ($15 \times 15 \times 1$ cm^3) and, at the bottom, a matrix of 3×3 lutetium-yttrium oxyorthosilicate inorganic scintillator crystals ($5 \times 5 \times 4$ cm^3). Finally, the detector is completed by an anticoincidence (VETO) system composed of five plastic scintillator planes completely surrounding the apparatus. The instrument is optimized to measure electrons in the 3–100 MeV energy range and protons with kinetic energy between 30 and 300 MeV, as well as light nuclei. The HEPD-01 capabilities in galactic, trapped, and solar proton measurements have already been shown in S. Bartocci et al. (2020), M. Martucci et al. (2023a), M. Martucci et al. (2023b), and M. Martucci et al. (2022). Furthermore, observations of variations of low-energy populations inside Earth's magnetosphere during geomagnetic storms can be found in F. Palma et al. (2021) and M. Piersanti et al. (2022). More technical details on the mission, detector, and data preparation are reported in P. Picozza et al. (2019), G. Ambrosi et al. (2020, 2021), and A. Sotgiu et al. (2020).

3. Daily Proton Fluxes

To study the ∼27 day GCR variation, daily proton fluxes from HEPD-01, EPHIN, ERNE, and AMS-02 were employed in the period between 2018 and 2019 August, where the abovementioned periodicity became more noticeable and stable. HEPD-01 proton fluxes were calculated directly from scratch, starting from calibrated level-2 data by the CSES/Limadou Collaboration. The selection criteria for the flux calculations in HEPD-01 are described in detail elsewhere, for example in S. Bartocci et al. (2020), and only a brief summary will be given here. HEPD-01 measurements are of a calorimetric nature, so only particles fully contained in the detector are considered to be valid. A system of VETO planes surrounding the payload ensures the containment and rejects secondary particles. The two upper layers of the TOWER (together with the information provided by the trigger plane) give the signal to start the chain of acquisition. Geometric factor, efficiencies, and systematics are all calculated using dedicated Geant4 simulations. To discriminate between protons coming from outside the magnetosphere and particles trapped inside, a static rigidity cutoff map—obtained using both the International Geomagnetic Reference Field and the Tsyganenko 96 magnetospheric model (N. A. Tsyganenko 1995; P. Alken et al. 2021)—was employed. Although HEPD-01 is switched off above ±65°, before entering the polar caps, the ∼60° aperture of the instrument allows good statistics in collecting galactic protons. On the other hand, level-2 EPHIN and ERNE data sets are publicly available on the OMNIWEB website,[26] while AMS-02 proton data time profiles are extracted from differential spectra reported in M. Aguilar et al. (2021). For EPHIN, we chose the 7–25 MeV channel (0.12–0.22 GV), for ERNE, we chose seven energy channels between 13 and 130 MeV (0.16–0.51 GV), while for AMS-02 we chose the range between 0.85 and 10.35 GV.

[26] https://omniweb.gsfc.nasa.gov/ftpbrowser/flux_spectr_m.html

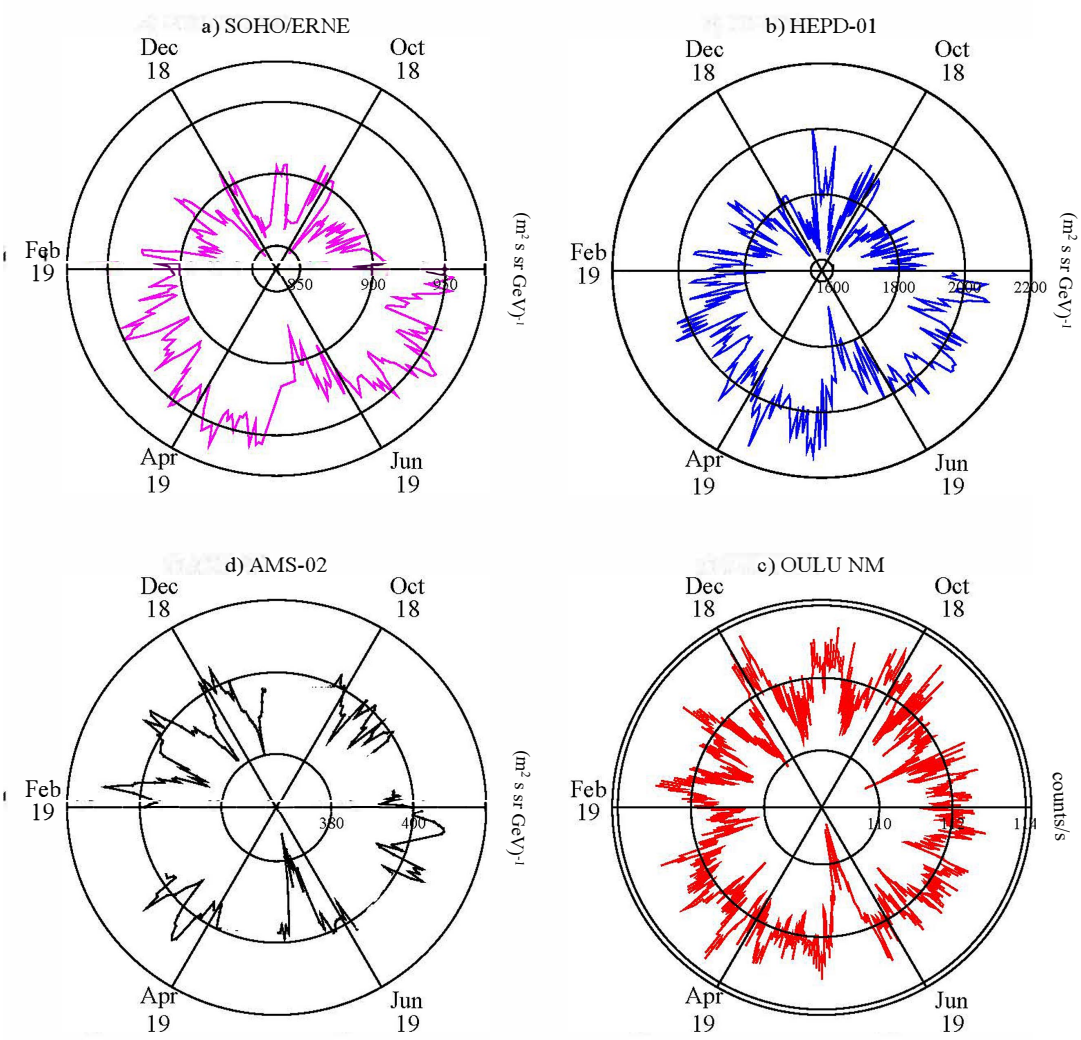

Figure 1. Daily proton fluxes as a function of time for ERNE (64–80 MeV), HEPD-01 (55–200 MeV), AMS-02 (2.7–3.0 GV), and daily count rates from the Oulu NM.

Finally, pressure and efficiency-corrected daily count rates from the Oulu NM—used in this work just as a reference for ground-based observations—were taken from NMDB Nest.[27] Daily proton fluxes as a function of time from ERNE (64–80 MeV or 0.35–0.40 GV), HEPD-01 (55–200 MeV or 0.33–0.63 GV), AMS-02 (2.7–3.0 GV), and daily count rates from the Oulu NM (estimated cutoff rigidity >0.81 GV) are reported in Figure 1.

To complete the picture of the ∼27 day variation, daily data from various proxies, such as the radial component of the HMF, SW speed, temperature, and proton density, were obtained from the OMNIWEB Data Explorer.[28]

4. Analysis and Results

To approach the study of the ∼27 day GCR variation, we followed the same approach as R. Modzelewska et al. (2020). Proton fluxes of HEPD-01, EPHIN, ERNE, and AMS-02 (as well as the count rates from the Oulu NM station) were detrended as displayed in the equation below:

$$y_{27} = \frac{(x - x_{27})}{x_{27}}, \quad (1)$$

where x_{27} is the extremal of the running 27 day average.

4.1. Classical Time-frequency Approach

To better investigate the dynamics of the temporal changes of this periodicity, the wavelet time-frequency spectrum technique was applied, adopting the Morlet wavelet mother function, see C. Torrence & G. P. Compo (1998). As examples, the detrended proton fluxes are presented for HEPD-01 (top panel in Figure 2), ERNE (top panel in Figure 3), and the Oulu NM (top panel in Figure 4), respectively. The results of the wavelet analysis of the daily proton flux by HEPD-01 (bottom panel in Figure 2), ERNE (bottom panel in Figure 3), and the Oulu NM (bottom panel in Figure 4) are depicted as well. Red, cross-hatched regions in the lower plots indicate the cone of influence where edge effects become important.

[27] https://www.nmdb.eu/nest/search.php
[28] https://omniweb.gsfc.nasa.gov/form/dx1.html

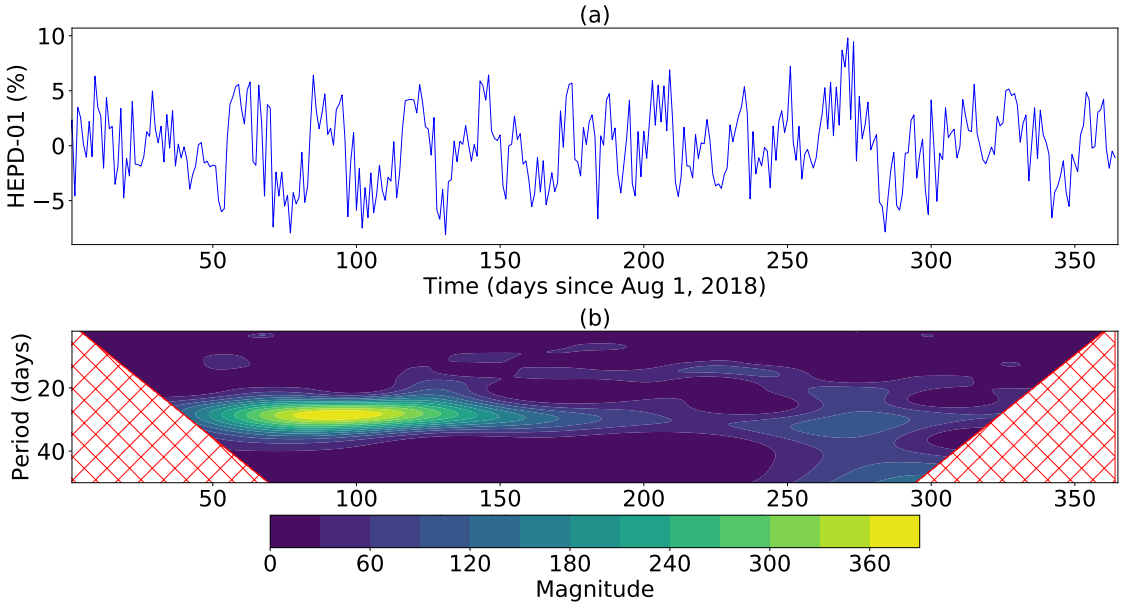

Figure 2. Top: temporal evaluation of the relative (detrended) proton fluxes measured by HEPD-01. Bottom: wavelet analysis of daily HEPD-01 proton flux for the 2018–2019 August period; cross-hatched regions on either end indicate the cone of influence where edge effects become important.

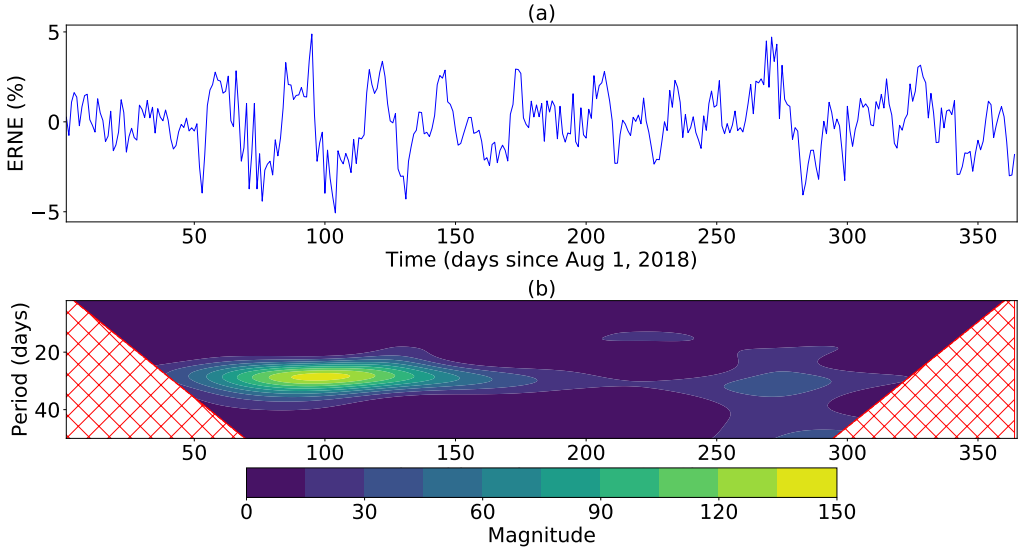

Figure 3. Top: temporal evaluation of the relative (detrended) proton fluxes measured by ERNE. Bottom: wavelet analysis of daily ERNE proton flux for the 2018–2019 August period; cross-hatched regions on either end indicate the cone of influence where edge effects become important.

Figure 5 depicts the strengths (normalized power) of four chosen rigidity intervals as a function of the period, averaged over the 2018–2019 August time window: 0.33–0.63 GV (a), 1.2–1.4 GV (b), 3.4–3.7 GV (c), and 7.3–8.0 GV (d). Profile (a) refers to HEPD-01, while profiles (b)–(d) are obtained from 3 AMS-02 channels. In all four distributions, the presence of the ∼27 day periodicity is evident and it is well above the 95% confidence level (red-dashed curves), estimated for a red-noise process with a lag-1 coefficient of 0.72. However, the strength changes as a function of rigidity, and the position of the various peaks is not always exactly at 27 days. Averaging over all the peak values (evaluated by performing a Gaussian fit around the maximum of each distribution) for all the available rigidities obtained from EPHIN, ERNE, HEPD-01, and AMS-02, we extracted a value of 27.3 ± 0.2 days. No other periodicities seem to stem from this analysis, or at least none of them are above the chosen confidence threshold.

Using the method adopted by R. Modzelewska & M. V. Alania (2013), we calculated the power (normalized for a better comparison of the shapes) of the ∼27 day variation as a function of time for the proton fluxes measured by HEPD-01 (0.33–0.63 GV), ERNE (0.35–0.40 GV), AMS-02 (2.7–3.0 GV), and Oulu. These profiles are reported in Figure 6 as blue, magenta, black, and red points, respectively. A Gaussian fit of the peak for each profile—performed to evaluate the position of this maximum—is superimposed as well.

The four profiles confirm the high power and large amplitude of the ∼27 day GCR variations in the period of 2018 September–2019 February, corresponding to

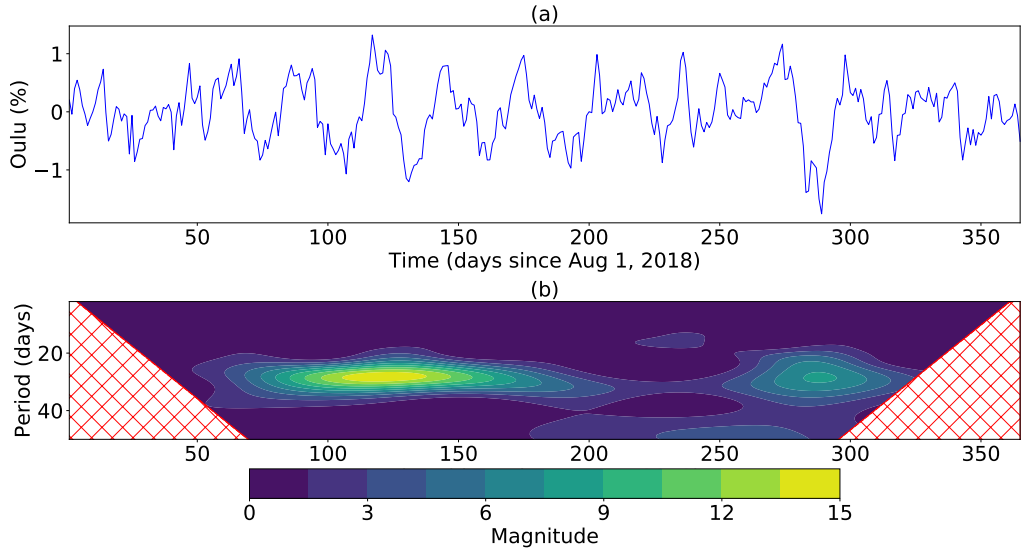

Figure 4. Top: temporal evaluation of the relative (detrended) count rates measured by the Oulu station. Bottom: wavelet analysis of daily Oulu count rates for the 2018–2019 August period; cross-hatched regions on either end indicate the cone of influence where edge effects become important.

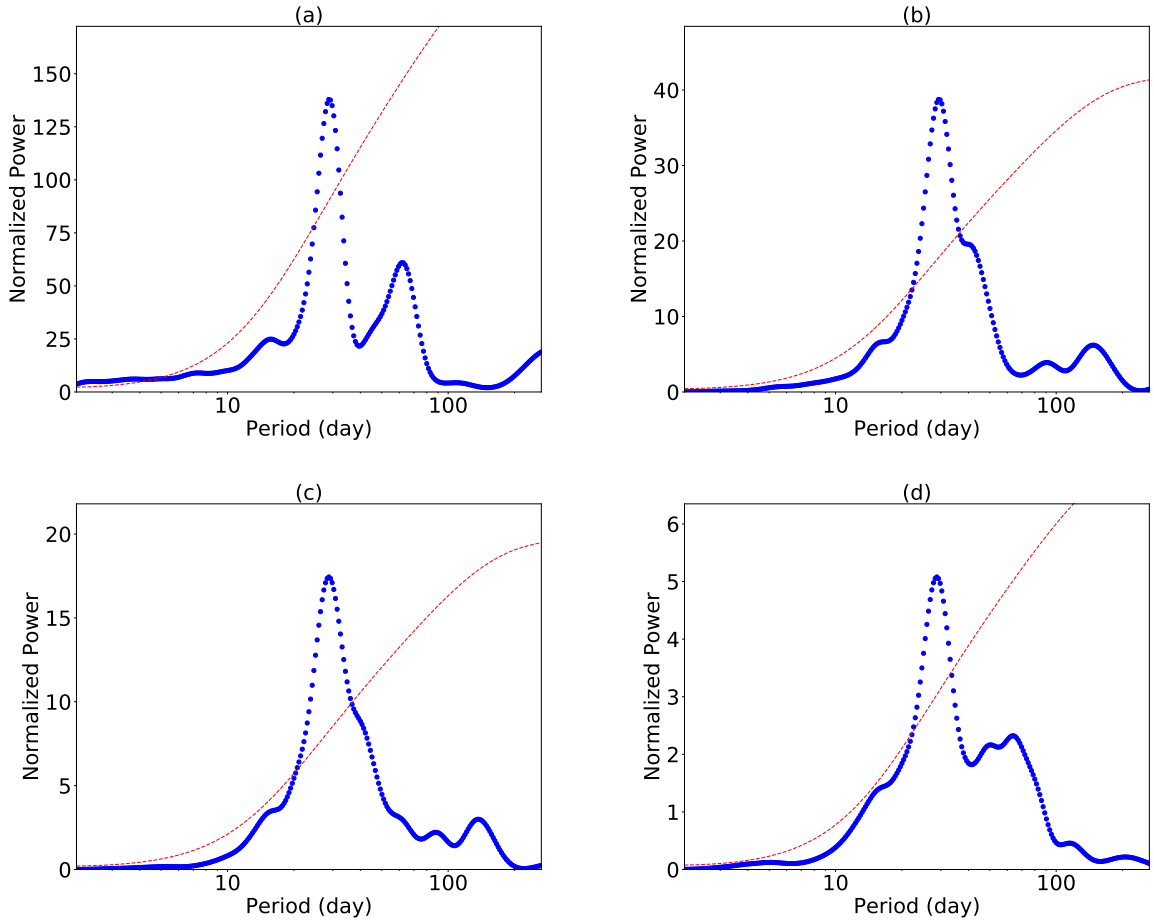

Figure 5. The normalized power spectra for four rigidity bins (blue markers) averaged over the period of 2018–2019 August: 0.33–0.63 GV (a), 1.2–1.4 GV (b), 3.4–3.7 GV (c), and 7.3–8.0 GV (d). Profile (a) refers to HEPD-01, while profiles (b)–(d) to AMS-02. The dashed red curves indicate the 95% confidence levels.

Carrington rotations (CRs) 2208–2214. The fit performed to extract the position of the maxima from these profiles gives the following results: 99.8 ± 2.7 days for ERNE, 94.6 ± 5.8 days for HEPD-01, 121.8 ± 18.6 days for Oulu, and 132.9 ± 13.6 days for AMS-02. This may imply a rigidity dependence of the occurrence of the maximum of the $\sim$27 day periodicity, which will be discussed in Section 5. Moreover, a much smaller second peak seemingly appears in all profiles after 2019 April–May, but in Oulu data, it shows a much greater power.

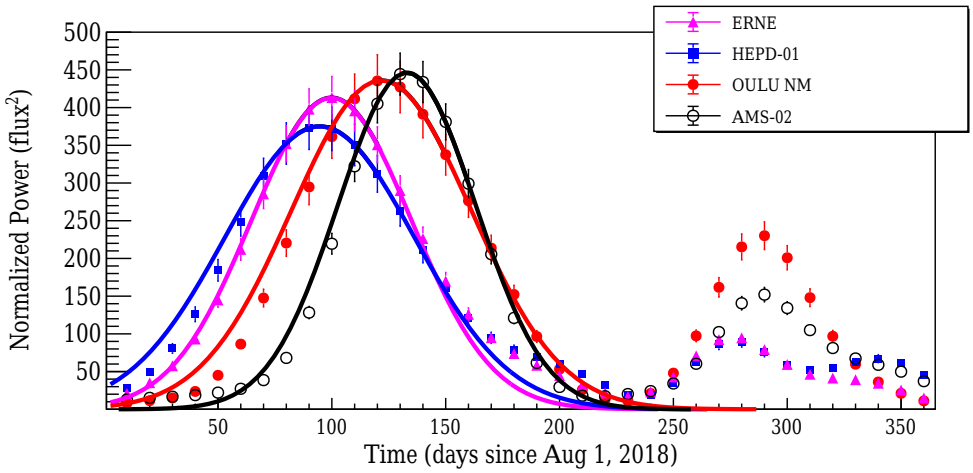

Figure 6. Normalized power of the recognized periodicity of ∼27 days for HEPD-01 (blue markers), ERNE (magenta markers), AMS-02 (black markers), and Oulu NM (red markers), for the 2018–2019 August period. A fit of the peak (solid lines) for each profile is also drawn.

4.2. Heliospheric and GCR Characteristic Features in 2018–2019

To further inspect the origin of the observed ∼27 day periodicity, the same time-frequency analysis was applied to relevant parameters of the HMF: the daily B_r (radial) component of the HMF, the SW velocity, the temperature, and the proton density. In Figure 7, the 2D results of the wavelet analysis are depicted. As expected (see A. Wawrzynczak et al. 2015; X. Guo & V. Florinski 2016; A. Kopp et al. 2017; X. Luo et al. 2020 and references therein), this ∼27 day signal is dominant in all of them and it roughly coincides with the signal extracted from HEPD-01, ERNE, AMS-02, and Oulu NM—see Figure 6. However, stable periodic variations in the SW speed, temperature, and proton density seem to start earlier with respect to the B_r component, and these ones last longer than in the GCRs.

Starting from 2018 September (CR 2208), the SW speed is showing a pronounced ∼27 day variation, connected with the same well-known variation in GCRs. Figure 8 gives a comparison of the 27 day variations in GCRs, in the SW, and in other heliospheric parameters during the period of 2018 September–2019 February. All time profiles have been detrended, as explained earlier. Furthermore, the first three CRs in this period (2208–210) are reported in the plot for clarity. It is interesting to note that there are two distinct peaks in the SW velocity (second panel from the top), separated by two valleys of rather distinct duration: a short one at the end of each CR, correlated with the fast crossing of the low-velocity layer surrounding the heliospheric current sheet (HCS), and the longer one appearing closer to the middle part of each CR, associated with the slow crossing of the HCS layer only slightly tilted to Earth's trajectory. This same configuration was seen in the 2008–2009 period, at the end of SC 23 (R. Modzelewska & A. Gil 2021). During the period under study, there were no interplanetary CMEs—as shown in the CDAW online catalog.[29]

4.3. The Fast Iterative Filtering Method and Validation

When analyzing nonstationary signals, traditional methods such as the (short time) Fourier transform and wavelet transform have been found insufficient for delivering detailed time-frequency information because of their inherent linearity. For this reason, research into new techniques for time-frequency analysis and signal decomposition has been ongoing for many years, resulting in the creation of numerous significant algorithms and methods, like the empirical mode decomposition (EMD; N. E. Huang et al. 1998). More recently, the iterative filtering (IF) algorithm and its generalizations have been introduced (L. Lin et al. 2009; A. Cicone et al. 2016; M. Piersanti et al. 2018). These methods rely on iterative processes and do not require any prior assumptions about the signal being analyzed. The structure of IF is similar to that of EMD. The main distinction lies in how the moving average of the signal is computed in IF, which involves convolving the signal $s(t)$ with a preselected filter function. This seemingly minor difference in the computation of the moving average between IF and EMD has enabled the mathematical analysis of IF (A. Cicone et al. 2016, 2019; A. Cicone 2020; A. Cicone & P. Dell'Acqua 2020; A. Cicone & H. Zhou 2021), including proofs of its convergence (A. Cicone et al. 2016; A. Cicone & H. Zhou 2021) and its acceleration in the form of the fast iterative filtering (FIF) method (A. Cicone 2020; A. Cicone & H. Zhou 2021). FIF achieves the same decomposition as IF when the signal is periodically extended at the boundaries. If the signal is not periodic at the boundaries, it can be pre-extended as needed to make it periodic at the new boundaries, as suggested by A. Stallone et al. (2020). FIF has been shown to be at least 2 orders of magnitude faster than any other iterative algorithm currently available for decomposing nonstationary signals, EMD included (A. Cicone 2020).

As a useful case study to prove its validity, in the present investigation, HEPD-01 proton data have been decomposed using FIF, according to the following equation:

$$\mathrm{HEPD01}(t) = \sum_{j=1}^{m} c_j(t) + r(t), \tag{2}$$

where m is the number of the obtained Intrinsic Mode Functions (IMFs), $c_j(t)$ is the generic IMF and $r(t)$ is the residue of the decomposition. Once decomposed, the IMF—characterized by a peculiar period of 27 days—has been

[29] https://cdaw.gsfc.nasa.gov/CME_list/radio/waves_type2.html

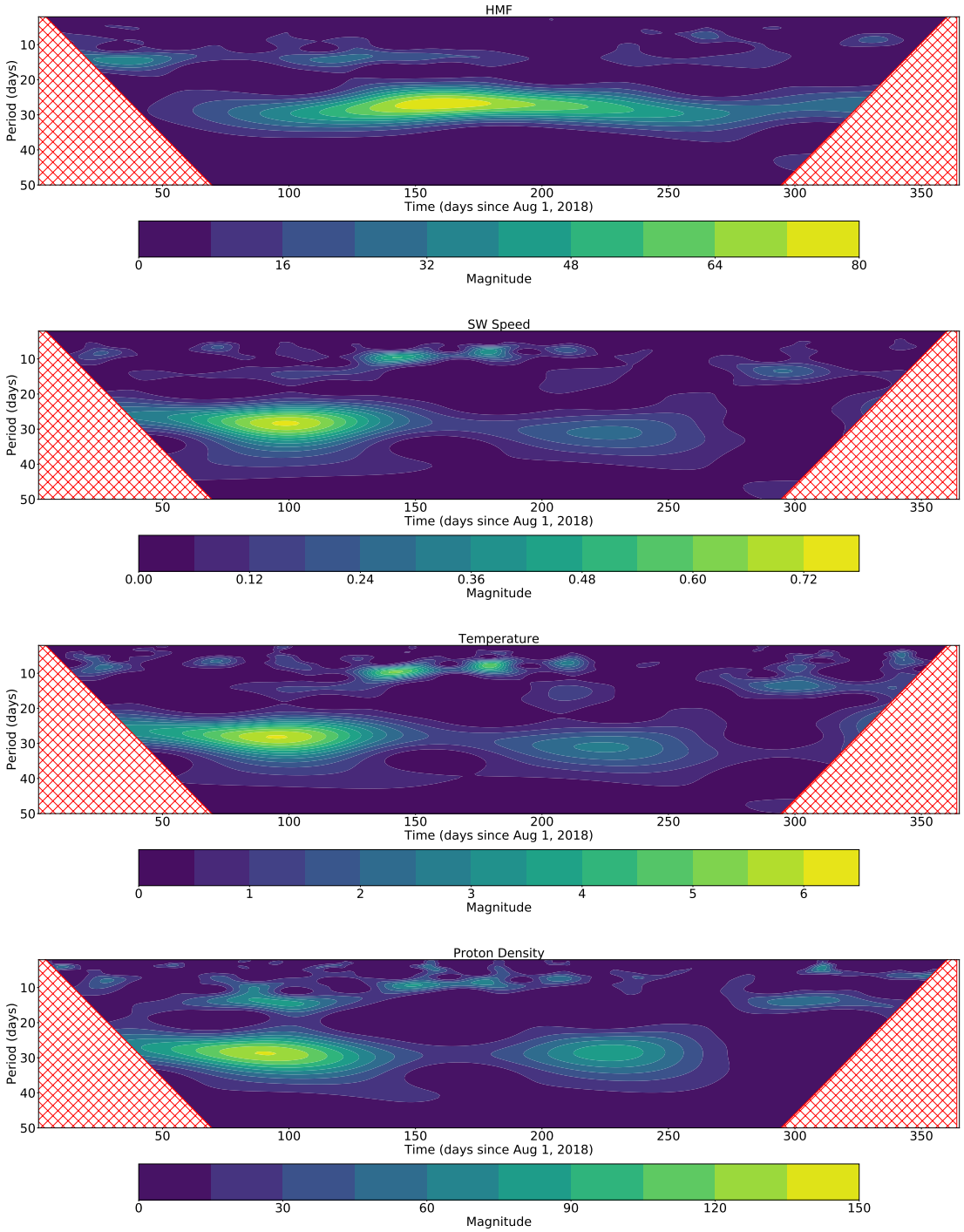

Figure 7. Results of the wavelet analysis for the daily B_r component of the HMF, the SW velocity, the temperature, and the proton density for the period of 2018–2019 August.

selected and analyzed in terms of amplitude and frequency modulation.

4.4. Rigidity Dependence of the 27 Day GCR Variation

We wanted to investigate the rigidity dependence of the amplitude of the ∼27 day GCR variation for proton fluxes; therefore, we used EPHIN, ERNE, HEPD-01, and AMS-02 data, introduced in Section 3, extending the rigidity interval from 0.12 to 10.35 GV mainly due to the capabilities and precision of the AMS-02 observations. For EPHIN, ERNE, and HEPD-01—which do not possess a magnetic spectrometer—the rigidity is calculated from the nominal extent of their energy channels employing the classical relation:

$$R = \frac{A}{Z} \times \sqrt{E_k^2 + 2E_k E_{k0}}, \tag{3}$$

where R is the rigidity, A is the mass number, Z is the charge, E_k is the kinetic energy per nucleon, and E_{k0} is the rest energy per nucleon.

The analysis was performed during the period of 2018 September–2019 February, where the ∼27 day periodicity was

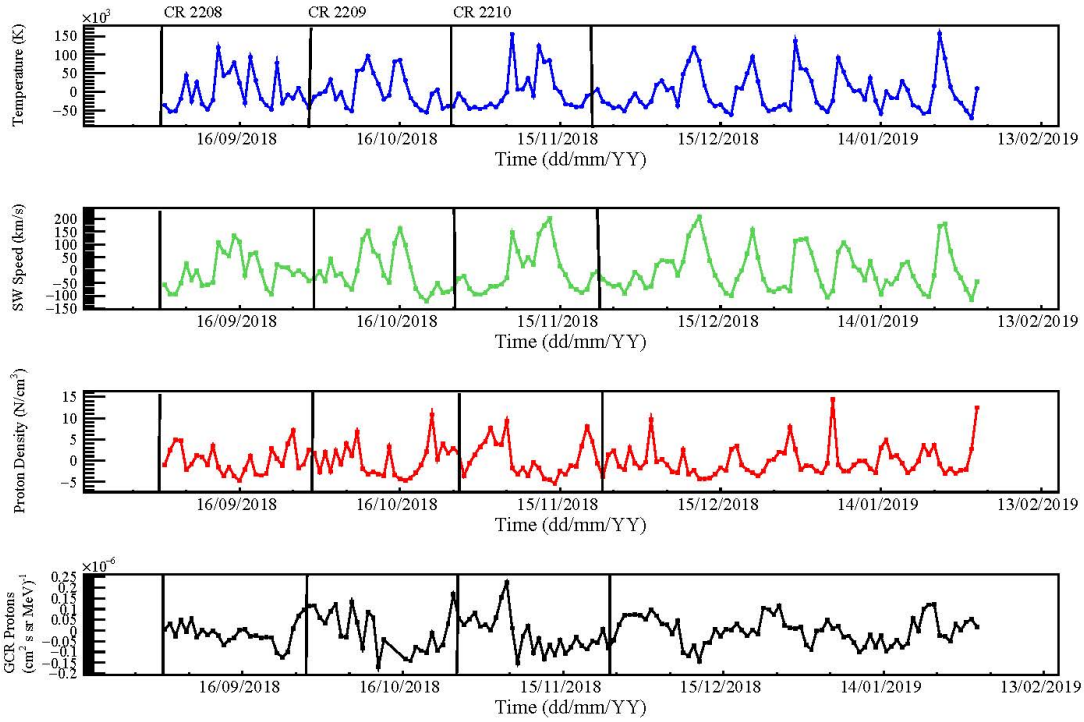

Figure 8. Relative detrended 27 day characteristics for the period of 2018 September–2019 February. From top to bottom: temperature, SW speed, proton density, and 55–200 MeV GCR protons from HEPD-01. The CRs 2208–2210 are indicated for clarity.

more evident and stable, as already discussed. The amplitude of the variation (A_{27} from now on) was extracted from a detrended five-day running average, while errors were calculated as the standard deviation. Figure 9 presents the values of A_{27} as a function of the magnetic rigidity R for proton fluxes observed by EPHIN (magenta marker), ERNE (green markers), HEPD-01 (blue and red markers), and AMS-02 (black markers) directly in space. For HEPD-01, the classical wavelet approach (see Section 4.1) and FIF (see Section 4.3) were used to extract a value of A_{27}.

The resulting distribution shows a nonmonotonic shape. For $R \gtrsim 0.8$ GV, it is a power law with index $\gamma = -0.48 \pm 0.17$ (see the dashed magenta line). However, it appears to flatten significantly below ∼0.8 GV, presenting a local minimum at ∼0.4 GV. It is important to note that the evaluation of A_{27} from the classical time-frequency analysis (blue circle) is in good agreement with that extracted from FIF (red square) for HEPD-01 within the error. It is worth noticing that this error is not instrumental but it is related to the dynamic of the amplitude of the ∼27 day component extracted with the FIF approach.

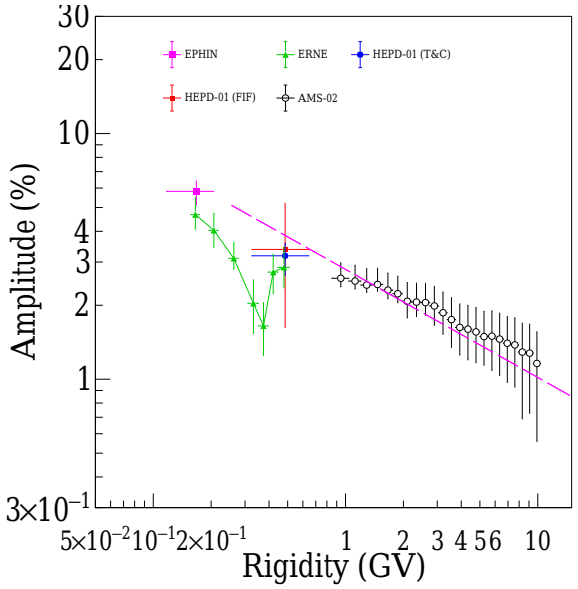

Figure 9. Reconstructed rigidity dependence of A_{27} for GCR proton data observed by EPHIN (magenta marker), ERNE (green markers), HEPD-01 (blue and red markers), and AMS-02 (black markers) from 2018 September to 2019 February. The dashed line represents the fit with a simple power law.

5. Discussion and Conclusions

We presented here a study of the recurrent ∼27 day variation of the GCR proton intensity between 2018 and 2019 August—during the solar minimum between SC 24 and SC 25—using data from various space-borne experiments such as EPHIN, ERNE, HEPD-01, AMS-02, and the Oulu NM. Using a classical time-frequency analysis with a Morlet mother function, we extracted the behavior of the magnitude and amplitude of this signal during the aforementioned period, resulting in a stronger presence of this variation in the few months between September 2018 and February 2019, see Figures 2, 3, and 4. This is justified by the fact that the rate of CIR occurrence is found to be high (∼33 yr^{-1} between 2015 and 2019)—see Figure 3 in R. Hajra & J. V. Sunny (2022). Moreover, the ∼27 day signal seems to be the only one strong enough to be above the 95% confidence level threshold, as can be seen in Figure 5. Other variations related to the synodic rotation period of the Sun (M. V. Alaniya & L. K. Shatashvili 1974; A. Gil & K. Mursula 2017), like the second harmonic (∼13.5 days) or the third one (∼9 days), are not present. This is in agreement with what was reported in P. Kotzé (2023).

The power of the ∼27 day variation as a function of time, depicted in Figure 6, shows a slight energy dependence, with the peak of the signal for AMS-02 and Oulu occurring later than the signal for HEPD-01 and ERNE. A similar behavior was found in Figure 3 of R. Modzelewska et al. (2020), where the peak in the signal from Oulu occurred later than the one from ARINA (0.43 GV or ∼80 MeV), while the peak extracted from PAMELA (1 GV or ∼430 MeV) is seemingly not shifted. This ARINA-Oulu shift is of the order of ∼30 days, consistent with our results, where the displacement between HEPD-01 (closer to the energy range of ARINA) and Oulu is about 27 ± 3 days.

Because the GCR recurrence is a consequence of solar rotation, we analyzed not only GCR fluxes, but also solar and heliospheric parameters to examine possible relations with the ∼27 day variations. The behavior of SW, temperature, proton density, and GCR intensity near Earth in the period of the intense signal can be considered as the manifestation of the steady but longitudinally dependent variations in the coordinate system rotating with the Sun (R. Modzelewska & A. Gil 2021). However, the GCR intensity (last panel of Figure 8) indicates a smoother shape in the ∼27 day variation, with a minimum formed around the aforementioned peaks of SW speed and a maximum around the long valley between the couple of peaks. This leads to the fact that there is no clear one-to-one correspondence between the variations in the GCR intensity and the heliospheric characteristics measured in near-Earth space. This is supported by the correlation factors ρ between the GCR intensity and the other proxies: $\rho = -0.58 \pm 0.03$ for the SW speed, $\rho = -0.54 \pm 0.04$ for the temperature, and $\rho = 0.16 \pm 0.02$ for the proton density. It is believed that the development of the ∼27 day variation in GCR profile needs a modulation region of several astronomical units in the radial direction for all longitudes and that the diffusion mechanism inside this enclosed region leads to a rather smoother shape of the ∼27 day wave (R. Modzelewska et al. 2020). On the other hand, the directly observed characteristic SW features are local, creating a mismatch with the shape of GCRs.

Regarding Figure 9, the rigidity distribution is in good agreement with what was found in R. Modzelewska et al. (2020) between 2007 and 2008 and S. A. Siruk et al. (2024) between 2015 and 2016—see Figures 7 and 12, respectively. The maximum around 1 GV was already reported by the Ulysses mission (R. B. McKibben et al. 1995; C. Paizis et al. 1999). In addition, Figure 9 presents a local minimum at ∼0.4 GV, which is probably caused by the particles accelerated by the CIR-driven shocks.

Originally, the behavior of A_{27} was interpreted in the framework of the force-field approximation, which does not allow for a clear explanation of the underlying physics, especially at lower energies. More recently, a novel approach is to adapt a magnetohydrodynamic model to simulate the background SW plasma with a CIR structure in the inner heliosphere—incorporated into a comprehensive Parker-type transport model (X. Luo et al. 2020, 2024). Numerical studies on the effects of a CIR on the propagation of GCR protons are also reported. Additionally, an empirical form is assumed for the rigidity dependence of the diffusion coefficient K, and the drift is also modified inside a CIR. As a result, the amplitude of the GCR variations—as introduced by a simulated CIR—revealed a peculiar energy dependence between 0.1 and 10 GV. Figure 10 in X. Luo et al. (2024) shows a distribution of A_{27} in qualitative agreement with our observations, with a flat behavior below ∼0.9 GV (together with a local minimum around 0.3 GV), and a decrease above this range. This is true despite that there is no acceleration of particles in the model used by X. Luo et al. (2024). By hypothesizing that the diffusion coefficient K scales as $\frac{1}{B}$ (where B is the magnetic field inside a CIR), then the CIR itself essentially behaves as a barrier against the diffusion of GCRs; as the radial distance increases, this effect becomes smaller. As a result, the model predicts a value for the power-law index of $\gamma = -0.438$ for protons, in very good agreement with the value we obtained in this work ($\gamma = -0.48 \pm 0.17$). This is remarkable despite the assumptions the model is based on, i.e., a common rigidity dependence between the components of the diffusion tensor K or the values assumed for the drift coefficient. In any case, our value of γ is very close to the one found in 2007–2008 ($\gamma = -0.51 \pm 0.11$) and in 2015–2016 (between $\gamma = -0.63 \pm 0.02$ and $\gamma = -0.93 \pm 0.03$).

In conclusion, we used data from various instruments to investigate the ∼27 day recurrent variation in GCR protons during the 2018–2019 period. In doing so, we also employed calibrated data from our particle detector (HEPD-01) below a few hundred MeV. Once again, HEPD-01 revealed itself as very well suited for studying galactic populations with high precision and stability, contributing to filling the gap between the high-energy observations from AMS-02 and the ones from EPHIN and ERNE at lower energies. In addition, in 2025 June, HEPD-02 (C. De Santis & S. Ricciarini 2022; U. Savino 2024) will be launched on board the new CSES satellite with increased energy and angular resolutions, a novel detection technique, and the possibility of detecting particles over polar caps; this will guarantee high observational capabilities even for years to come.

Acknowledgments

This work makes use of data from the CSES mission, a project funded by China National Space Administration (CNSA), China Earthquake Administration (CEA), in collaboration with the Italian Space Agency (ASI), National Institute for Nuclear Physics (INFN), Institute for Applied Physics (IFAC-CNR), and Institute for Space Astrophysics and Planetology (INAF-IAPS). This work was supported by the Italian Space Agency in the framework of the "Accordo Attuativo 2020-32.HH.0 Limadou Scienza+" (CUP F19C20000110005), the ASI-INFN Agreement No. n.2014-037-R.0, addendum 2014-037-R-1-2017, and the ASI-INFN Agreement No. 2021-43-HH.0. We also acknowledge the support and hospitality provided by the Institute for Fundamental Physics of the Universe - IFPU (Trieste, Italy) that contributed to the development of this work and financial support from the Italian foreign minister in the context of "Programma Esecutivo Italia–Sud Africa" (code ZA23MO02).

ORCID iDs

R. Battiston https://orcid.org/0000-0002-5808-7239
D. Campana https://orcid.org/0000-0003-1504-9707
M. Cristoforetti https://orcid.org/0000-0002-0127-1342
C. De Donato https://orcid.org/0000-0002-9725-1281
C. De Santis https://orcid.org/0000-0002-7280-2446
A. Di Luca https://orcid.org/0000-0002-9074-2133
F. M. Follega https://orcid.org/0000-0003-2317-9560

G. Gebbia https://orcid.org/0000-0001-7252-7416
A. Lega https://orcid.org/0000-0002-1660-0524
M. Martucci https://orcid.org/0000-0002-3033-4824
G. Masciantonio https://orcid.org/0000-0002-8911-1561
M. Mese https://orcid.org/0000-0003-1452-3542
C. Neubüser https://orcid.org/0000-0002-2008-8404
F. Nozzoli https://orcid.org/0000-0002-4355-7947
A. Oliva https://orcid.org/0000-0002-6612-6170
G. Osteria https://orcid.org/0000-0002-9871-8103
A. Perinelli https://orcid.org/0000-0001-5603-3950
P. Picozza https://orcid.org/0000-0002-7986-3321
E. Ricci https://orcid.org/0000-0002-4222-9976
M. Ricci https://orcid.org/0000-0001-6816-4894
S. B. Ricciarini https://orcid.org/0000-0001-6176-3368
Z. Sahnoun https://orcid.org/0000-0003-1176-2003
U. Savino https://orcid.org/0000-0003-1884-2444
V. Scotti https://orcid.org/0000-0003-3253-2805
R. Sparvoli https://orcid.org/0000-0002-6314-6117
P. Ubertini https://orcid.org/0000-0003-0601-0261
V. Vilona https://orcid.org/0000-0001-9893-9419
P. Zuccon https://orcid.org/0000-0001-6132-754X
M. Boezio https://orcid.org/0000-0002-8015-2981
R. Munini https://orcid.org/0000-0001-7598-1825
O. P. M. Aslam https://orcid.org/0000-0001-9521-3874
X. Luo https://orcid.org/0000-0002-4508-6042
M. D. Ngobeni https://orcid.org/0000-0001-5844-3419
M. S. Potgieter https://orcid.org/0000-0003-0793-7333

References

Aguilar, M., Cavasonza, L. A., Ambrosi, G., et al. 2021, PhRvL, 127, 271102
Alaniya, M. V., & Shatashvili, L. K. 1974, Quasi-periodical Variations of Cosmic Rays (Tbilisi: Metsniereba)
Alken, P., Thébault, E., Beggan, C. D., et al. 2021, EP&S, 73, 49
Ambrosi, G., Bartocci, S., Basara, L., et al. 2020, NIMPA, 974, 164170
Ambrosi, G., Bartocci, S., Basara, L., et al. 2021, NIMPA, 1013, 165639
Bakaldin, A., Batishchev, A., Voronov, S., et al. 2007, CosRe, 45, 445
Bartocci, S., Battiston, R., Burger, W. J., et al. 2020, ApJ, 901, 8
Bazilevskaya, G., Broomhall, A. M., Elsworth, Y., & Nakariakov, V. M. 2014, SSRv, 186, 359
Bigazzi, A., & Ruzmaikin, A. 2004, ApJ, 604, 944
Cane, H. V. 2000, SSRv, 93, 55
Chowdhury, P., Kudela, K., & Moon, Y. J. 2016, SoPh, 291, 581
Cicone, A. 2020, NuAlg, 85, 811
Cicone, A., & Dell'Acqua, P. 2020, JCoAM, 373, 112248
Cicone, A., Garoni, C., & Serra-Capizzano, S. 2019, Linear Algebra Its Appl., 580, 62
Cicone, A., Liu, J., & Zhou, H. 2016, Appl. Comput. Harmon. Anal., 41, 384
Cicone, A., & Zhou, H. 2021, NuMat, 147, 1
De Santis, C., & Ricciarini, S. 2022, ICRC (Berlin), 395, 058
Decker, R. 1999, ICRC (Salt Lake City, UT), 7, 512
Forbush, S. E. 1938, TrAGU, 19, 193
Gil, A., & Alania, M. V. 2013, SoPh, 283, 565
Gil, A., & Mursula, K. 2017, A&A, 599, A112
Guo, X., & Florinski, V. 2016, ApJ, 826, 65
Hajra, R., & Sunny, J. V. 2022, SoPh, 297, 30
Hathaway, D. H. 2015, LRSP, 12, 4
Heber, B., & Potgieter, M. S. 2006, SSRv, 127, 117
Heber, B., Sanderson, T. R., & Zhang, M. 1999, AdSpR, 23, 567
Huang, N. E., Shen, Z., Long, S. R., et al. 1998, RSPSA, 454, 903
Kopp, A., Wiengarten, T., Fichtner, H., et al. 2017, ApJ, 837, 37
Kotzé, P. 2023, SoPh, 298, 107
Krieger, A. S., Timothy, A. F., & Roelof, E. C. 1973, SoPh, 29, 505
Kudela, K., & Sabbah, I. 2015, ScChE, 59, 547
Kunow, H., Dröge, W., Heber, B., et al. 1995, SSRv, 72, 397
Lin, L., Wang, Y., & Zhou, H. 2009, Adv. Adapt. Data Anal., 01, 543
Luo, X., Potgieter, M. S., Zhang, M., & Shen, F. 2024, ApJ, 961, 21
Luo, X., Zhang, M., Feng, X., et al. 2020, ApJ, 899, 90
López-Comazzi, A., & Blanco, J. 2022, ApJ, 927, 155
Martucci, M., Ammendola, R., Badoni, D., et al. 2023a, ApJL, 945, L39
Martucci, M., Bartocci, S., Battiston, R., et al. 2022, PhRvD, 105, 062001
Martucci, M., Laurenza, M., Benella, S., et al. 2023b, SpWea, 21, e2022SW003191
McKibben, R. B., Simpson, J. A., Zhang, M., Bame, S., & Balogh, A. 1995, SSRv, 72, 403
Modzelewska, R., & Alania, M. V. 2013, SoPh, 286, 593
Modzelewska, R., Bazilevskaya, G. A., Boezio, M., et al. 2020, ApJ, 904, 3
Modzelewska, R., & Gil, A. 2021, A&A, 646, A128
Neugebauer, M., & Snyder, C. W. 1966, JGR, 71, 4469
Paizis, C., Heber, B., Ferrando, P., et al. 1999, JGR, 104, 28241
Palma, F., Sotgiu, A., Parmentier, A., et al. 2021, ApSci, 11, 5680
Parker, E. N. 1965, P&SS, 13, 9
Phillips, J., Bame, S., Feldman, W., et al. 1995, Sci, 268, 1030
Picozza, P., Battiston, R., Ambrosi, G., et al. 2019, ApJS, 243, 16
Picozza, P., Galper, A., Castellini, G., et al. 2007, APh, 27, 296
Piersanti, M., Del Moro, D., Parmentier, A., et al. 2022, SpWea, 20, e2021SW003016
Piersanti, M., Materassi, M., Cicone, A., et al. 2018, JGRA, 123, 1031
Potgieter, M. S. 2013a, LRSP, 10, 3
Potgieter, M. S. 2013b, SSRv, 176, 165
Potgieter, M. S. 2017, AdSpR, 60, 848
Raphaldini, B., Dikpati, M., & McIntosh, S. 2023, SPD, 55, 2023n7i102p05
Richardson, I. G. 2004, SSRv, 111, 267
Richardson, I. G. 2018, LRSP, 15, 1
Richardson, I. G., Cane, H. V., & Wibberenz, G. 1999, JGR, 104, 12549
Savino, U. 2024, NIMPA, 1063, 169281
Shen, X., Zhang, X., Yuan, S., et al. 2018, ScChE, 61, 634
Simpson, J. A. 1998, SSRv, 83, 169
Siruk, S. A., Kuznetsov, A. V., Mayorov, A. G., & Yulbarisov, R. F. 2024, AdSpR, 74, 1978
Smith, E. J., & Wolfe, J. H. 1976, GeoRL, 3, 137
Sotgiu, A., De Donato, C., Fornaro, C., et al. 2020, Softw. Pract. Exper., 51, 1459
Stallone, A., Cicone, A., & Materassi, M. 2020, NatSR, 10, 15161
Torrence, C., & Compo, G. P. 1998, BAMS, 79, 61
Tsurutani, B., Gonzalez, W., Gonzalez, A., et al. 2006, JGR, 111, A07S01
Tsyganenko, N. A. 1995, JGR, 100, 5599
Usoskin, I. G. 2017, LRSP, 14, 3
Wawrzynczak, A., Modzelewska, R., & Gil, A. 2015, JPhCS, 574, 012078
Wiengarten, T., Oughton, S., Engelbrecht, N. E., et al. 2016, ApJ, 833, 17